**Supporting Information: The effect of nanoparticulate PdO co-catalysts on the Faradaic and light conversion efficiency of WO₃ photoanodes for water oxidation**

Anna A. Wilson[a], Sacha Corby[a], Laia Francàs*[b], James R. Durrant[a], Andreas Kafizas*[a,c,d]

[a] Department of Chemistry and Centre for Plastic Electronics, Imperial College London, White City Campus, London, W12 0BZ, UK

[b] Departament de Química, Universitat Autònoma de Barcelona, Cerdanyola del Vallès, Barcelona 08193, Spain

[c] The Grantham Institute, Imperial College London, South Kensington, London, SW7 2AZ, UK

[d] London Centre for Nanotechnology, Imperial College London, SW7 2AZ, UK
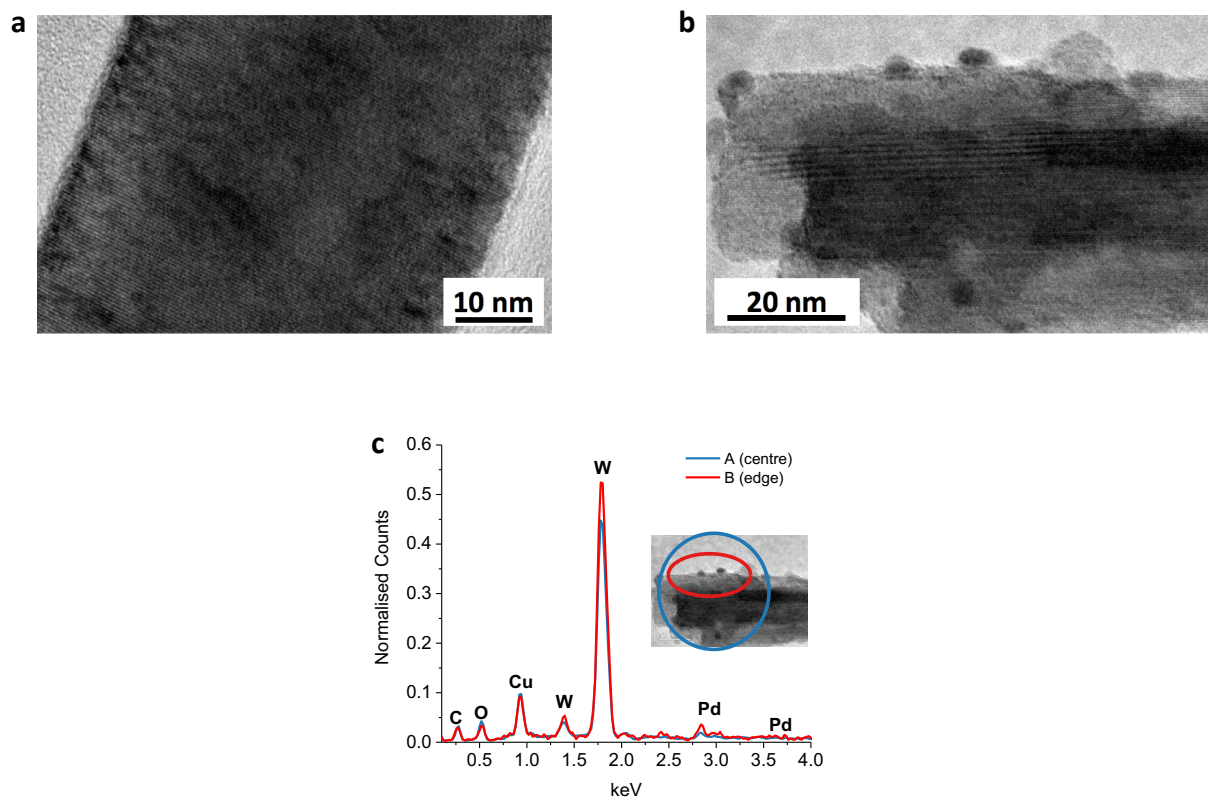
Figure S1. HR-TEM images of a) a bare WO₃ nanoneedle, b) Pd nanoparticles on WO₃ (Pd(A)/WO₃), and c) EDX for two points on Pd(A)/WO₃ (note that the Cu signal is from the TEM grid). Where Pd NPs are observed, there is an even dispersion of NPs across the nanoneedle surface. However, there is variation between nanoneedles of the same film, whereby Pd NPs are not observed on all nanoneedles. This is rationalised by the WO₃ film morphology and the Pd deposition conditions, whereby the dense nature of the WO₃ film, together with the laminar aerosol flow through the reaction chamber, inhibits the infiltration of Pd NPs throughout the coating, and thus limits Pd deposition to the upper region of the nanoneedles.
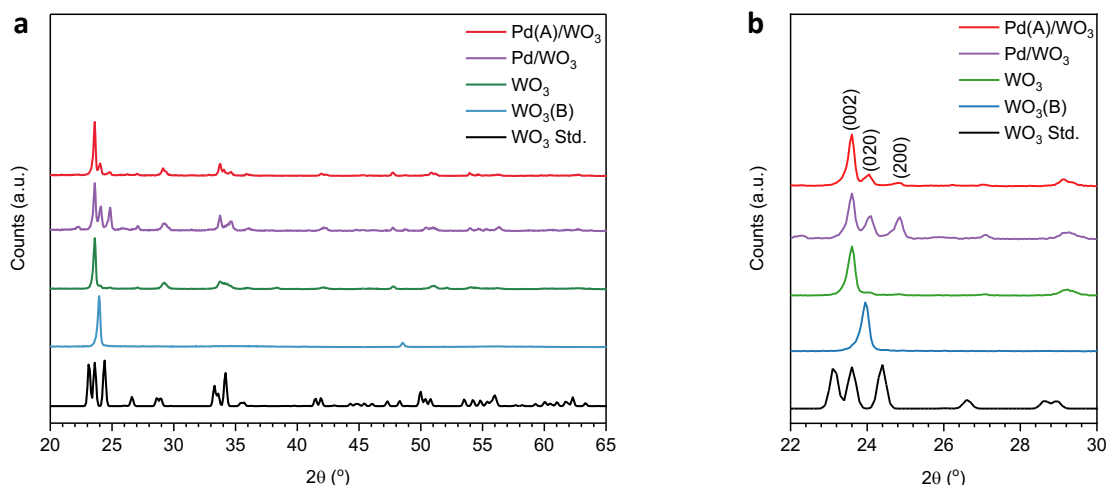
Figure S2. X-Ray diffraction (XRD) patterns of the synthesised films compared to database values for a $WO_3$ standard. The defined peaks of all films correspond to crystalline monoclinic $WO_3$ (space group $P2_1/n$) with a = 7.3008 Å, b = 7.5389 Å, c = 7.6896 Å and β = 90.892° (ICDS no. 80056) as typical unit cell parameters. The (002) peak dominates for all photoanodes, with the (020) and (200) peaks also visible for $Pd/WO_3$ and $Pd(A)/WO_3$. The monoclinic structure extends to photoanodes with Pd NPs and confirms that the addition of a co-catalyst did not alter the crystal structure of $WO_3$. Relative to the non-annealed $WO_3(B)$, the peaks for $WO_3$-based materials are shifted to higher diffraction angles, indicative of a reduced unit cell size that is rationalised by a lattice contraction due to a decrease in oxygen vacancies.
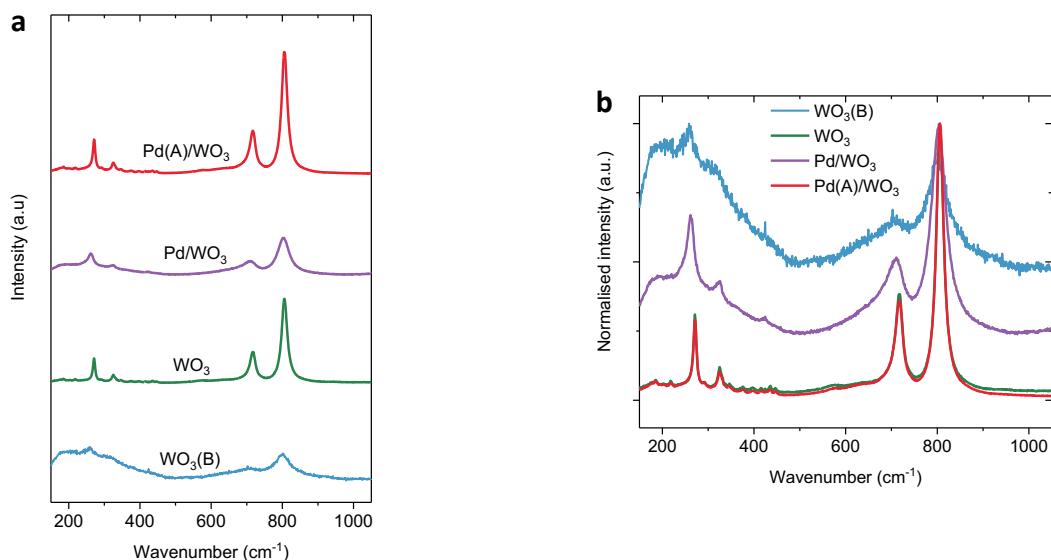


Figure S3. a) Raman spectra of the as-synthesised photoanodes, b) Raman spectra normalised to the peak intensities in the 800-808 $cm^{-1}$ region and overlayed. The broad and diffuse peaks in the $WO_3(B)$ spectrum likely mask spectral features and are frequently observed for oxygen deficient $WO_3$ materials due to the significant contribution of both $W^{5+}$-O and $W^{6+}$-O vibrational modes,[10,11] as expected here. The deposition of Pd NPs onto $WO_3$ to obtain $Pd/WO_3$ results in a degree of peak broadening (although the peak definition remains more notable than for $WO_3(B)$), however, $Pd(A)/WO_3$ exhibits well defined peaks analogous to those of $WO_3$ (see normalised spectra). The second AA-CVD step required to deposit Pd likely introduces carbon residues from the organic precursors that reduce peak definition and are removed by the annealing treatment.
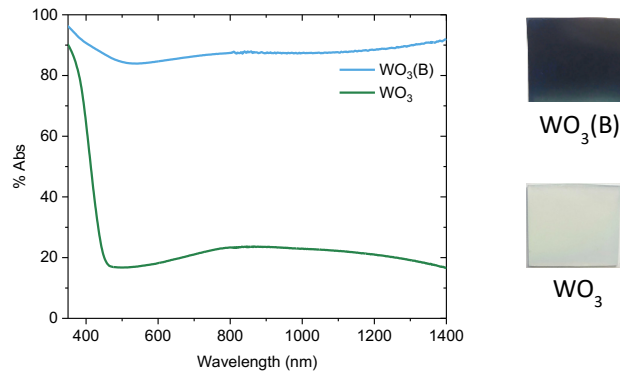
Figure S4. UV-Vis absorption spectra of as-synthesised $WO_3(B)$ prior to annealing and $WO_3$ following annealing, in addition to photographs of the films showing the distinct colour change from dark blue to creamy white, that occurs with the decrease in near-IR absorption.
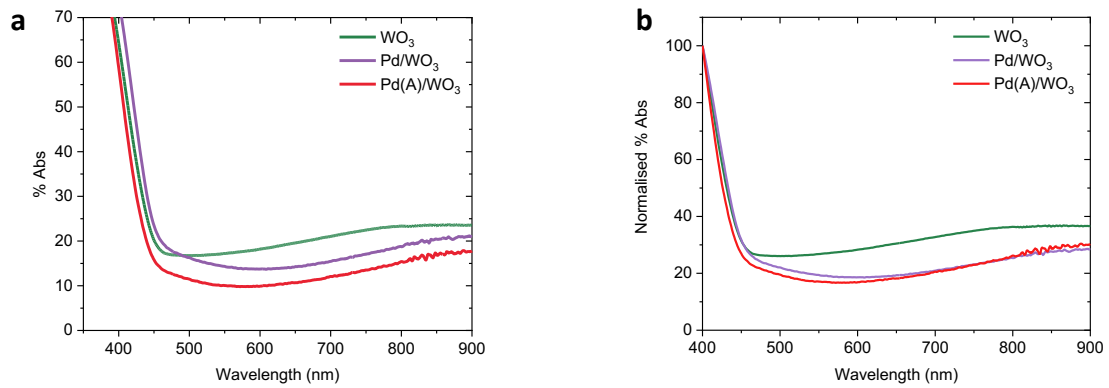


Figure S5. a) UV-Vis absorption spectra of $WO_3$, $Pd/WO_3$ and $Pd(A)/WO_3$ photoanodes, b) UV-Vis spectra normalised at 400 nm where band gap absorption occurs, to directly compare the near-IR absorption properties.
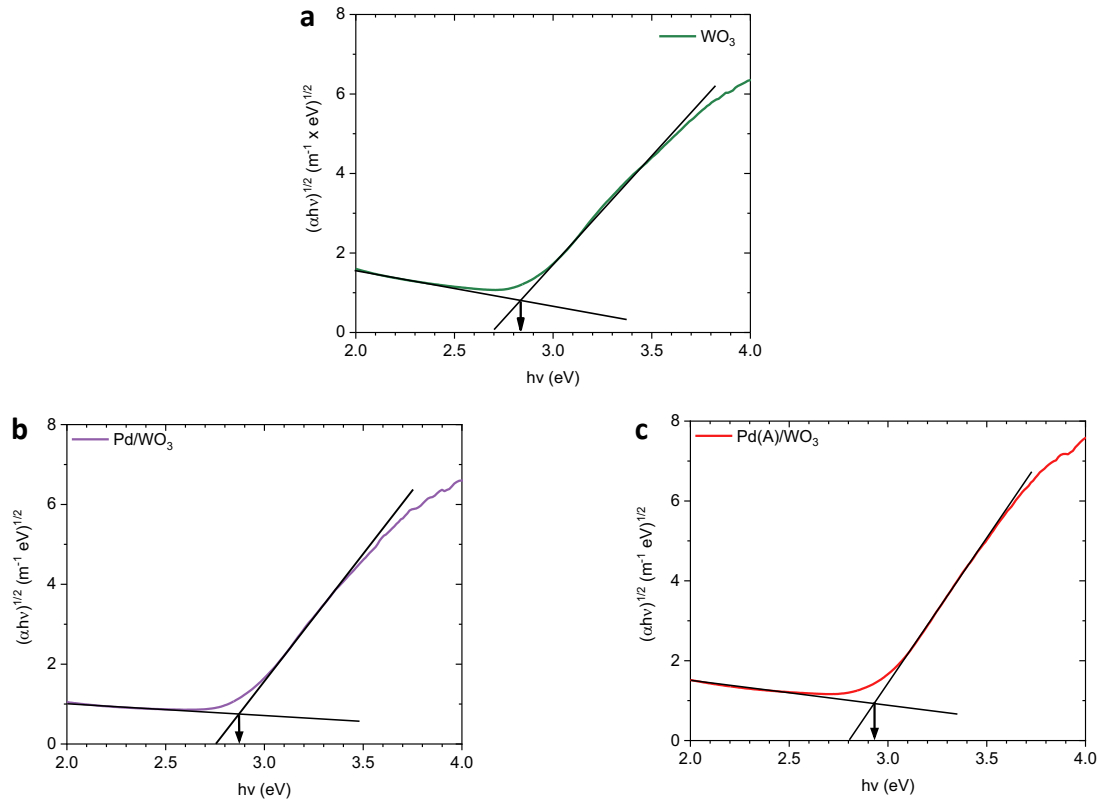
Figure S6. Tauc plots of $(\alpha h\nu)^{1/2}$ *vs.* $h\nu$ to give band gap energy estimations for a) $WO_3$, b) $Pd/WO_3$ and c) $Pd(A)/WO_3$.
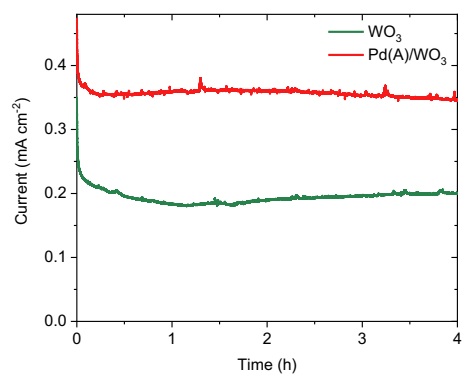
Figure S7: Stability of photocurrent generation at 1.23 $V_{RHE}$ over a 4-hour period (simulated 1 sun AM 1.5G irradiance).
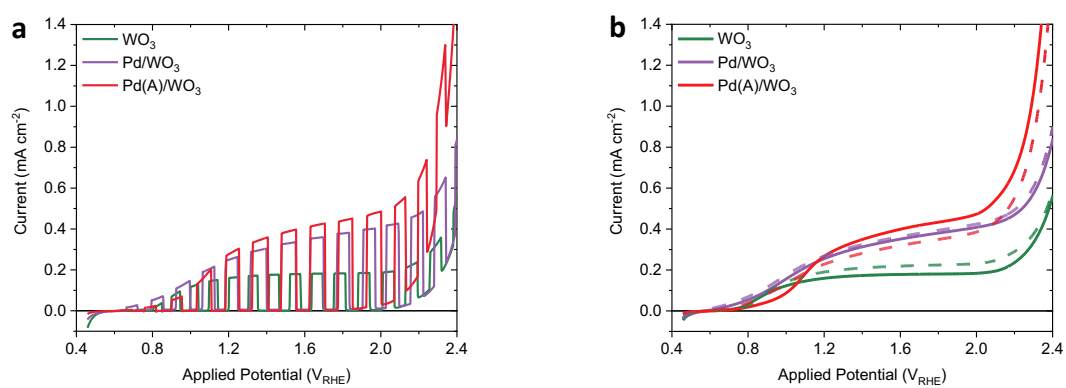


Figure S8. LSV measurements using simulated 1 sun AM 1.5G irradiation a) for chopped-light conditions under front illumination and b) comparing current generation under front (solid line) and back illumination (dashed line).
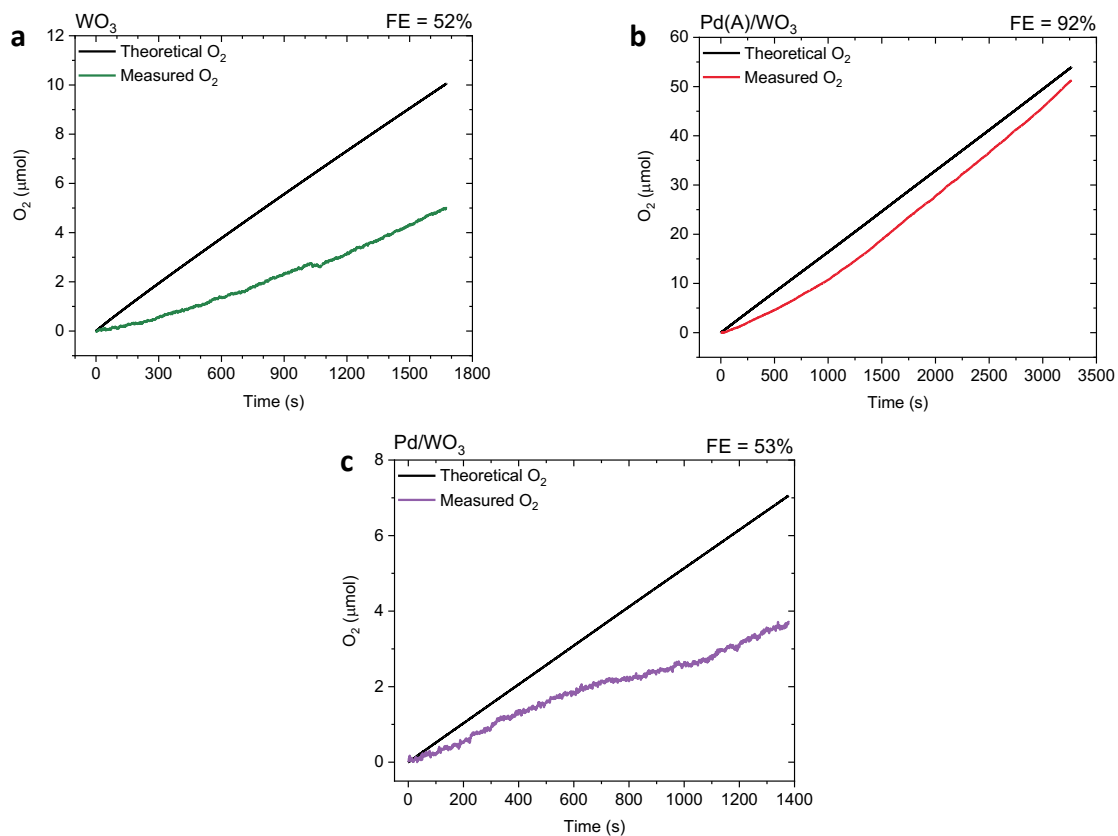
Figure S9. FE measurements comparing the selectivity of water oxidation for a) WO₃, b) Pd/WO₃, and c) Pd(A)/WO₃, photoanodes at 1.23 $V_{RHE}$ in 0.1 M $H_2SO_4$, irradiated with a 365 nm LED mimicking the photon flux that would be absorbed at 1 sun irradiance. $O_2$ evolution is measured in the gas phase using a Clark electrode and the theoretical $O_2$ yield at 100% FE is calculated from the integrated photocurrent density obtained over the course of the experiment.

Figure S10: Predicted electronic band structure before and after Fermi level equilibrium for a) Pd/WO₃ and b) Pd(A)/WO₃, obtained using a AFORS.HET model[12] with the parameters outlined in Table S4. The model predicts the effects of Pd oxidation state on band bending in WO₃ and does not take into account the effects of band bending at the electrolyte interfaces or applied potential.
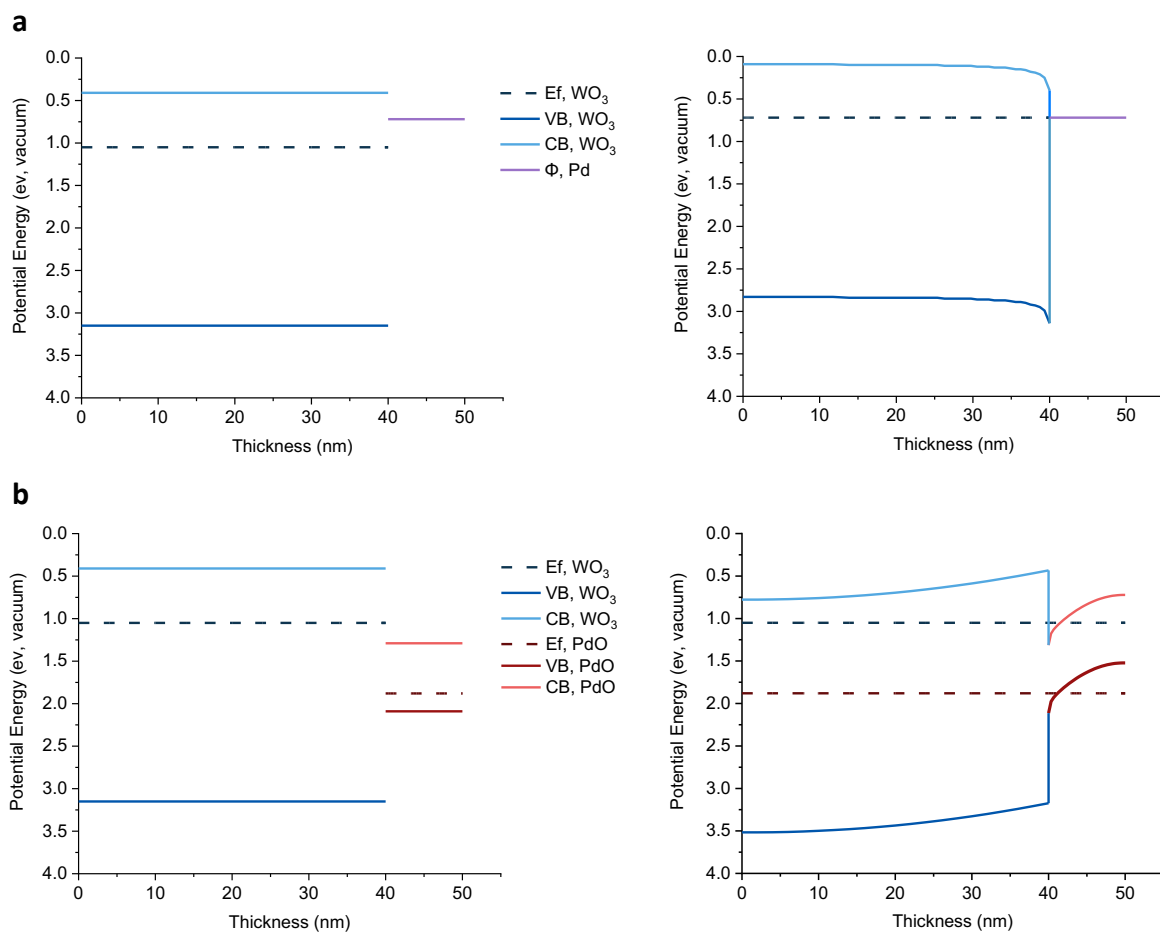
Table S1. A comparison of the oxygen states that are vacant, calculated from the ratios of $W^{5+}$ to $W^{6+}$ states, in addition to the relative quantities of carbon residues present

| Entry | Photoanode | % $W^{5+}$ vs. $W^{6+}$ [a] | % Oxygen vacancy states[b] | % C vs. W[c] |
|---|---|---|---|---|
| 1 | $WO_3$ | 7.77 | 1.30 | 0.62 |
| 2 | $Pd/WO_3$ | 6.20 | 1.03 | 0.87 |
| 3 | $Pd(A)/WO_3$ | 6.37 | 1.06 | 0.66 |

[a]Ratio calculated using the $W^{5+}$ and $W^{6+}$ peak areas in the W 4f scan. [b]Calculated by dividing '% $W^{5+}$ vs. $W^{6+}$' by six, to account for each W site being associated with three oxygen sites, each with a charge of -2. [c]Ratio calculated using the total fitted peak areas of the C 1s and W 4f scans.


Table S2: A comparison of the photocurrents associated with $WO_3$, $Pd/WO_3$ and $Pd(A)/WO_3$ photoanodes obtained from TSP calculations and LSV measurements.

| | $WO_3$ | $Pd/WO_3$ | $Pd(A)/ WO_3$ |
|---|---|---|---|
| TSP (mA cm$^{-2}$) | 0.78 | 0.89 | 1.22 |
| LSV photocurrent (mA cm$^{-2}$) | 0.16 | 0.22 | 0.28 |


Table S3. Comparison of the effects of PdO addition on the FE of $WO_3$ compared to alternative $WO_3$ modifications

| Entry | Photoanode | $WO_3$ FE / % | Modified $WO_3$ FE / % | FE Increase (Change) / % | Ref. |
|---|---|---|---|---|---|
| 1 | $Pd(A)/WO_3$[a] | 52 | 92 | 40 (77) | This work |
| 2 | $FeOOH/WO_3$[b] | 27 | 96 | 69 (256) | 1 |
| 3 | $Cr_2O_3/WO_3$[c] | 74 | 92 | 18 (24) | 2 |
| 4 | $Al_2O_3 /WO_3$[d] | 50 | 80 | 30 (60) | 3 |

[a]0.1 M $H_2SO_4$, 1.23 $V_{RHE}$, 365 nm LED (~1 sun); [b]0.1 M $KPO_4$ buffer solution (pH 4), 1.34 $V_{RHE}$, 2 sun 200 mW cm$^{-2}$ AM 1.5G illumination; [c]0.1 M $Na_2SO_4$, 1.0 $V_{RHE}$, 1 sun 100 mW cm$^{-2}$ AM 1.5G illumination; [d]0.1 M $H_2SO_4$ , 1.23 $V_{RHE}$, 1 sun 100 mW cm$^{-2}$ AM 1.5G illumination.


Table S4: Parameters used for the band bending models in Figure S10.

| | Thickness (nm) [a] | Donor density (cm$^{-3}$) | Electron affinity/ Workfunction (eV) | $E_{bg}$ (eV) | Density (g cm$^{-3}$) | Dielectric constant | Ref. |
|---|---|---|---|---|---|---|---|
| $WO_3$ | 40 | $-2.50 \times 10^{19}$ | 4.91 | 2.74 | 7.16 | 1000 | 4 |
| PdO | 10 | $4.20 \times 10^{18}$ | 5.79 | 0.8 | 8.3 | 8 | 5–7 |
| Pd | 10 | very high | 5.22 | 0 | 11.9 | 2.5 | 8,9 |

[a]The thickness of the $WO_3$ nanoneedles and Pd-based nanoparticles were taken from the SEM and TEM images respectively.

## References

1    C. R. Lhermitte, J. Garret Verwer and B. M. Bartlett, *J. Mater. Chem. A*, 2016, **4**, 2960–2968.

2    Z. Hu, M. Xu, Z. Shen and J. C. Yu, *J. Mater. Chem. A*, 2015, **3**, 14046–14053.

3    C. Fàbrega, S. Murcia-López, D. Monllor-Satoca, J. D. Prades, M. D. Hernández-Alonso, G. Penelas, J. R. Morante and T. Andreu, *Appl. Catal. B Environ.*, 2016, **189**, 133–140.

4    C. Sotelo-Vazquez, R. Quesada-Cabrera, M. Ling, D. O. Scanlon, A. Kafizas, P. K. Thakur, T.-L. Lee, A. Taylor, G. W. Watson, R. G. Palgrave, J. R. Durrant, C. S. Blackman and I. P. Parkin, *Adv. Funct. Mater.*, 2017, **27**, 1605413.

5    O. García-Serrano, A. Andraca-Adame, R. Baca-Arroyo, R. Peña-Sierra and G. Romero-Paredes R., *CCE 2011 - 2011 8th Int. Conf. Electr. Eng. Comput. Sci. Autom. Control. Progr. Abstr. B.*, , DOI:10.1109/ICEEE.2011.6106122.

6    X. Yong and M. A. A. Schoonen, *Am. Mineral.*, 2000, **85**, 543–556.

7    P. O. Nilsson and M. S. Shivaraman, *J. Phys. C Solid State Phys.*, 1979, **12**, 1423–1427.

8    Electron Work Function of the Elements, https://public.wsu.edu/~pchemlab/documents/Work-functionvalues.pdf, (accessed 2 April 2020).

9    W. E. Vargas, *Appl. Opt.*, 2017, **56**, 1266.

10   N. Xue, R. J. Yu, C. Z. Yuan, X. Xie, Y. F. Jiang, H. Y. Zhou, T. Y. Cheang and A. W. Xu, *RSC Adv.*, 2017, **7**, 2351–2357.

11   S. Liu, J. Gong, X. Chang, C. Li, A. Li, J. Zhang and T. Wang, *J. Mater. Chem. A*, 2017, **6**, 3350–3354.

12   R. Varache, C. Leendertz, M. E. Gueunier-Farret, J. Haschke, D. Muñoz and L. Korte, *Sol. Energy Mater. Sol. Cells*, 2015, **141**, 14–23.